Engineering Science & Technology
https://ojs.wiserpub.com/index.php/EST/

Research Article

Topological Optimization Design of Automobile Suspension Swing Arm Based on PEEK Material

Junxian Wang[1], **Xiaochi Wang**[2*], **Yang Gao**[2], **Jian Zhang**[2], **Yuxin Lin**[3], **Wanjia Wang**[2]

[1]School of Materials Science and Engineering, Dalian Jiaotong University, Dalian, 116028, China
[2]School of Mechanical Engineering, Dalian Jiaotong University, Dalian, 116028, China
[3]School of Rail Intelligent Engineering, Dalian Jiaotong University, Dalian, 116028, China
E-mail: wangxiaochi@djtu.edu.cn

Received: 27 October 2025; **Revised:** 25 December 2025; **Accepted:** 31 December 2025

Abstract: To achieve a lightweight design of the vehicle suspension lower control arm under complex road load conditions, a topology optimization model based on the variable-density method was established, with the structural stiffness of the suspension system during vehicle operation as the constraint and minimum mass as the objective. Based on the optimization results, the structure of the lower control arm was redesigned, and stiffness and strength checks were performed within the designated design region. The original steel material was replaced with lower-density Polyether Ether Ketone (PEEK), and the complex geometry was manufactured using Fused Deposition Modeling (FDM), increasing the feasibility of realizing the topology-optimized design. In this study, only material specimens underwent physical testing; the final control arm was not experimentally tested and was evaluated solely through simulation. Because FDM forming quality is influenced by printing parameters, tensile tests were conducted on PEEK specimens printed under different parameter settings, and the optimal parameters were determined to be a layer height of 0.2 mm, a build-plate temperature of 120 °C, and a tetrahedral infill pattern. Specimens printed under these optimal conditions were subsequently subjected to thermal-holding treatments to investigate the effects of different heat-holding processes on tensile strength. By comparing mechanical properties before and after heat treatment, the optimal condition was identified as 340 °C for 2 hours. A multibody dynamics simulation was employed to determine the actual loading conditions of the lower control arm during vehicle operation. Static structural analysis of the maximum load case was then performed to identify stress concentrations and guide the topology optimization. Under the requirement of maintaining adequate mechanical performance, material usage was minimized, ultimately reducing the mass of the lower control arm by 49.05% and achieving substantial lightweighting.

***Keywords*:** Polyether Ether Ketone (PEEK), fused deposition, multibody dynamics, topology optimization

1. Introduction

The automotive suspension lower control arm is a critical load-bearing and guiding component that connects the wheel to the vehicle body. It is typically located at the bottom of the front or rear suspension and is responsible for supporting wheel loads as well as transmitting various impacts and moments from the wheel during vehicle operation [1], as illustrated in Figure 1. Through ball-joint connections and bushing pairs, the lower control arm enables relative

DOI: https://doi.org/10.37256/est.7120269008

rotational motion between the wheel and the vehicle body, while withstanding complex longitudinal, lateral, and vertical impact loads during acceleration, braking, cornering, and traversing uneven road surfaces. In addition, under high-speed driving or emergency braking conditions, the control arm must resist transient impacts and vibrations caused by changes in vehicle attitude, imposing stringent requirements on the material's mechanical strength, fatigue resistance, and impact performance. At present, lower control arms are predominantly manufactured from cast iron or high-strength steel to ensure sufficient stiffness and durability under complex loading conditions. However, although cast iron is easy to process, its relatively low impact toughness makes it prone to fatigue damage under alternating loads and vibration. High-strength steel provides excellent strength but has high density and weight, which is unfavorable for achieving vehicle lightweighting objectives. As the automotive industry evolves, lightweight design has become a central focus of vehicle structural engineering due to its direct impact on fuel economy, power performance, and handling stability.

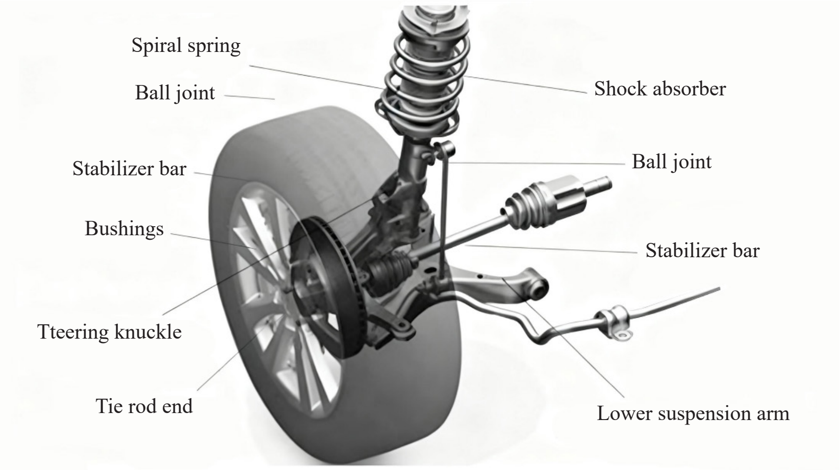

Figure 1. Composition diagram of a suspension system of an automobile [1]

The development of lightweight design has advanced alongside progress in computational technologies and structural optimization methods, shifting from simple weight-reduction strategies to integrated design concepts that combine structural optimization with material innovation. Modern lightweight design emphasizes not only material selection but also the balance between mechanical performance and weight reduction achieved through structural optimization [2]. Among optimization methods, topology optimization has been widely adopted because it enables optimal material distribution under given loads and boundary conditions. Unlike size or shape optimization, topology optimization reconfigures the internal structural layout, determining the optimal distribution and dimensions of voids to reduce material usage without compromising strength or stiffness [3]. Combined with 3D printing technology, topology optimization overcomes the limitations of conventional manufacturing and enables rapid fabrication of complex structures, making it increasingly applicable to suspension components, chassis structures, and other high-load automotive parts [4].

In terms of material innovation, the high-performance engineering polymer Polyether Ether Ketone (PEEK) offers a promising pathway for structural lightweighting. PEEK exhibits excellent properties, including high strength, high stiffness, fatigue resistance, corrosion resistance, thermal stability, and self-lubrication. Its density is only one-third that of traditional cast iron, while its mechanical strength can even surpass that of certain metallic materials [5]. However, it should be noted that applying PEEK to a lower control arm—a key component subjected to complex alternating loads—also presents several potential issues that warrant careful consideration. Compared with steel or ductile iron, the creep resistance of PEEK may degrade significantly under long-term high-load conditions. In particular, continuous bending and torsional loads may lead to slow dimensional changes, thereby affecting the suspension's alignment accuracy. Although PEEK exhibits relatively high tensile strength, its impact toughness remains lower than that of most metallic materials, making it more susceptible to brittle fracture under high-speed impacts or large-displacement shock loads. Therefore, a comprehensive evaluation of its long-term creep behavior and impact resistance is essential before practical application. Therefore, using PEEK for the structural fabrication of the lower control arm can significantly reduce weight while maintaining adequate mechanical performance. PEEK is well suited for manufacturing complex geometries through Fused Deposition Modeling (FDM), which greatly enhances the feasibility of realizing topology-optimized designs. FDM is a representative additive manufacturing technology that forms three-dimensional solid parts by heating and melting the material and depositing it layer by layer along a predefined path [6]. It offers a variety of forming modes, with infill patterns such as cubic, tetrahedral, honeycomb, and grid structures. Owing to its low equipment cost and high processing flexibility, FDM is suitable for producing automotive components with complex geometries and high precision requirements.

The quality of FDM-fabricated parts has a substantial influence on their mechanical properties. To determine the optimal printing process, tensile tests were performed on PEEK specimens produced under different FDM parameters, and the optimal printing conditions were identified as a layer height of 0.2 mm, a build-plate temperature of 120 °C, and a tetrahedral infill pattern. The printed specimens were subsequently subjected to heat treatment at 340 °C for 2 hours to enhance their tensile strength and structural stability. However, existing research processes often treat printing-parameter optimization, structural simulation, and engineering validation as separate stages, lacking an integrated and systematic methodology. As a result, the coupling mechanisms among material properties, printing processes, and topology-optimized structures remain insufficiently understood, leaving a gap in the theoretical foundation. This constitutes a key scientific issue in current lightweight suspension component research, as it directly affects the reliability of optimization outcomes and their engineering applicability. Subsequently, multibody dynamics simulations were conducted to analyze the load distribution of the suspension lower control arm under various road and driving conditions—such as straight-line driving, cornering, and emergency braking—to identify regions of maximum equivalent stress. However, existing studies on "load acquisition procedures" often remain limited to idealized operating conditions, such as isolated steering or braking scenarios, without establishing a comprehensive load-spectrum generation method that incorporates multivariable driving behavior, road excitations, and tire models. This limitation leads to discrepancies between simulated and actual loading conditions. Developing an integrated loading workflow that includes multibody dynamics, road roughness models, and transient tire-road interactions is therefore essential for improving the realism of topology optimization and its engineering applicability. This gap also defines one of the core issues addressed in the present study. Building upon this foundation, topology optimization was employed to redesign the lower control arm, aiming to minimize material usage while ensuring that stiffness and strength remain uncompromised, thereby achieving efficient lightweighting. Based on the aforementioned limitations in current methodologies, this study proposes a fully coupled "material-manufacturing-dynamic loading-topology optimization" workflow. This approach addresses key challenges in traditional research, including oversimplified loading conditions, the disconnect between structural optimization and manufacturing constraints, and the inadequate linkage between material performance and simulation. As such, the study demonstrates a clear problem-oriented focus and notable methodological innovation.

2. Related theories

2.1 *Principle of multibody dynamics*

The Inspire software was used to perform dynamic simulations of the opening and closing motion of the automotive suspension lower control arm. Analyzing the kinematic characteristics of a multibody system composed of rigid bodies involves the fundamental steps of consistently deriving the system's differential-algebraic equations of motion [7]. In this context, understanding the individual motion of the different rigid bodies that constitute the multibody system plays a central role. For a rigid-body multibody system, the kinematics of each rigid body are fully defined with respect to a body-fixed reference frame. Accordingly, the local positions of the particles belonging to the rigid body are described relative to this fixed reference frame. The mathematical tool used for this purpose is referred to as the fundamental equations of rigid-body kinematics, which are defined as follows:

$$r(P) = R + A\overline{u}(P)$$

$$= R + u(P) \tag{1}$$

where $r(P)$ is the global position vector of the material point P attached to the rigid body, R represents the global position vector of the object's fixed reference frame origin, and $\overline{u}(P)$ is the local position vector of the material point P. A is the rotation matrix of the rigid body, and $u(P)$ is the global position vector of the material point P. In addition, the velocity and acceleration fields of rigid bodies can be easily determined in analytical form by calculating the first and second derivatives of the rigid body position field relative to the time variable. To do this, it can be written as:

$$\begin{aligned} v(P) &= \dot{r}(P) \\ &= \dot{R} + \omega \times u(P) \\ &= \dot{R} + A(\overline{\omega} \times \overline{u}(P)) \end{aligned} \tag{2}$$

It can also be written as:

$$\begin{aligned} a(P) &= \ddot{r}(P) \\ &= \ddot{R} + \dot{\omega} \times u(P) + \omega \times (\omega \times u(P)) \\ &= \ddot{R} + A(\dot{\overline{\omega}} \times \overline{u}(P)) + A(\overline{\omega} \times (\overline{\omega} \times \overline{u}(P))) \end{aligned} \tag{3}$$

Where $v(P)$ and $a(P)$ denote the velocity and acceleration fields of the rigid body, respectively, while ω and $\overline{\omega}$ represent the global and local angular velocity vectors of the rigid body, respectively. Although the second equation is mathematically equivalent to the first, it is more convenient for describing the kinematics of complex multibody systems. Furthermore, it can be readily shown that the velocity and acceleration fields of a rigid body can be expressed as linear functions of the generalized velocities and accelerations, respectively. Accordingly, they can be written as follows:

$$\begin{aligned} v(P) &= \dot{r}(P) = L(P)\dot{q} \\ a(P) &= \ddot{r}(P) \\ &= L(P)\ddot{q} + \dot{L}(P)\dot{q} \end{aligned} \tag{4}$$

Where q is the system generalized coordinate vector, $L(P)$ the Jacobian matrix representing the position field of the rigid body, given by the following equation:

$$L(P) = \begin{bmatrix} I & A\tilde{u}^T(P)\overline{G} \end{bmatrix} \tag{5}$$

Where $\tilde{u}^T(P)$ is the transformation matrix with each local position vector (P) and G, which allows the local angular velocity vector of a rigid body to be written as a linear combination of the object's rotational coordinates.

3. Methods and preparation processes

3.1 *PEEK specimen preparation and tensile test*

3.1.1 *Preparation before printing*

The test specimens were modeled using the three-dimensional design software SolidWorks. Tensile specimens were dimensioned according to International Organization for Standardization (ISO) 527-1A, with the I-type dumbbell specimen used as the reference geometry [8]. The resulting 3D models were exported in STereoLithography (STL) format, and the specific dimensions of the tensile specimens are shown in Figure 2. Slicing and printing parameters were set using Ultimaker Cura software, after which the specimens were fabricated using a 3D printer. Prior to printing, PEEK was dried at 160 °C for 2 hours and stored in a dry environment. Initially, the printing method was selected as the variable among the FDM process parameters, and the corresponding tensile specimens were printed in a randomized order. The main FDM process parameters were: nozzle diameter of 0.4 mm, nozzle temperature of 430 °C, and 100% infill density [9]. To prevent warping during printing, a layer of solid adhesive was applied to the build platform. This coating ensured that the extruded molten PEEK filament adhered better to the platform, promoting improved bonding between successive layers of PEEK during printing.

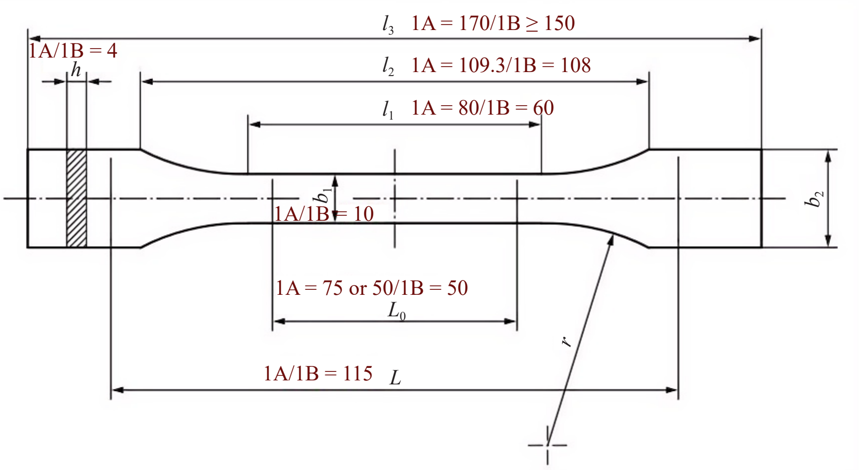

Figure 2. The specific size of the stretched part

3.1.2 *Sample preparation*

Import the STL file of the stretched part into the software to set specific printing parameters. The specific printing parameters are as follows: printing speed is 40 mm/s, nozzle diameter is 0.4 mm, printing temperature is 440 °C, printer cabin temperature is 50 °C, printing platform temperature is 120 °C, layer thickness is 0.1 mm, 0.2 mm, 0.3 mm, and filling rate is 100%. The effect of the filling method on the mechanical properties of PEEK was verified by setting different filling methods. The specific settings are as follows (Table 1).

Specimens printed with different infill patterns and layer heights exhibit varying tensile strengths [10]. For instance, grid infill employs a linear cross-arrangement, forming a regular internal grid structure that provides relatively uniform support and strength. Concentric circular infill generates internal layers in the form of concentric rings; this ring structure enhances mechanical performance by effectively distributing external loads, making it particularly suitable for components that require uniform load-bearing. This infill pattern can provide relatively high strength, especially on the load-bearing surfaces. However, concentric circular infill may not achieve optimal interlayer adhesion during printing and cannot reach 100% infill, as shown in Figure 3. Figure 4 illustrates the printing process of the tensile specimens.

Table 1. Printing parameter settings

Sample	Floor height/mm	Platform temperature, °C	Filling method
1	0.1	120	Cube
2	0.1	120	Concentric circles
3	0.1	120	Grid
4	0.1	120	Tetrahedron
5	0.2	120	Cube
6	0.2	120	Concentric circles
7	0.2	120	Grid
8	0.2	120	Tetrahedron
9	0.3	120	Cube
10	0.3	120	Concentric circles
11	0.3	120	Grid
12	0.3	120	Tetrahedron

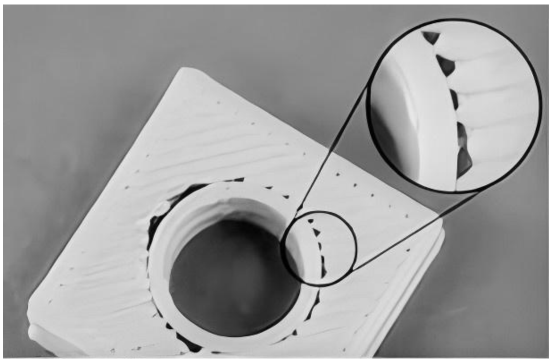

Figure 3. The concentric circles do not adhere well to each other

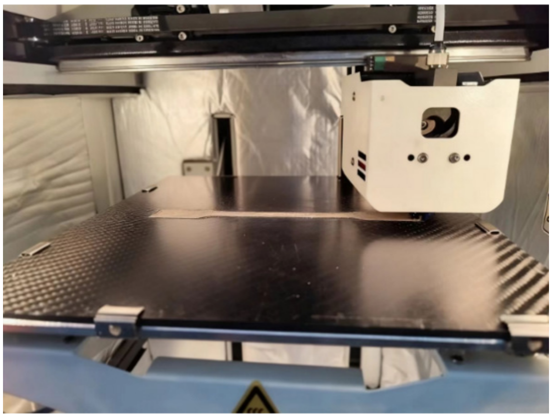

Figure 4. Printing of test specimens

3.1.3 *Stretching of the test piece*

The tensile test is carried out in accordance with the ISO 527 standard. The initial distance of the clamping spacing is set to 115 mm, the measured length is 50 mm, and the tensile speed is 0.5 mm/min. The specific tensile test process is shown in Figure 5.

Figure 5. Tensile experiment

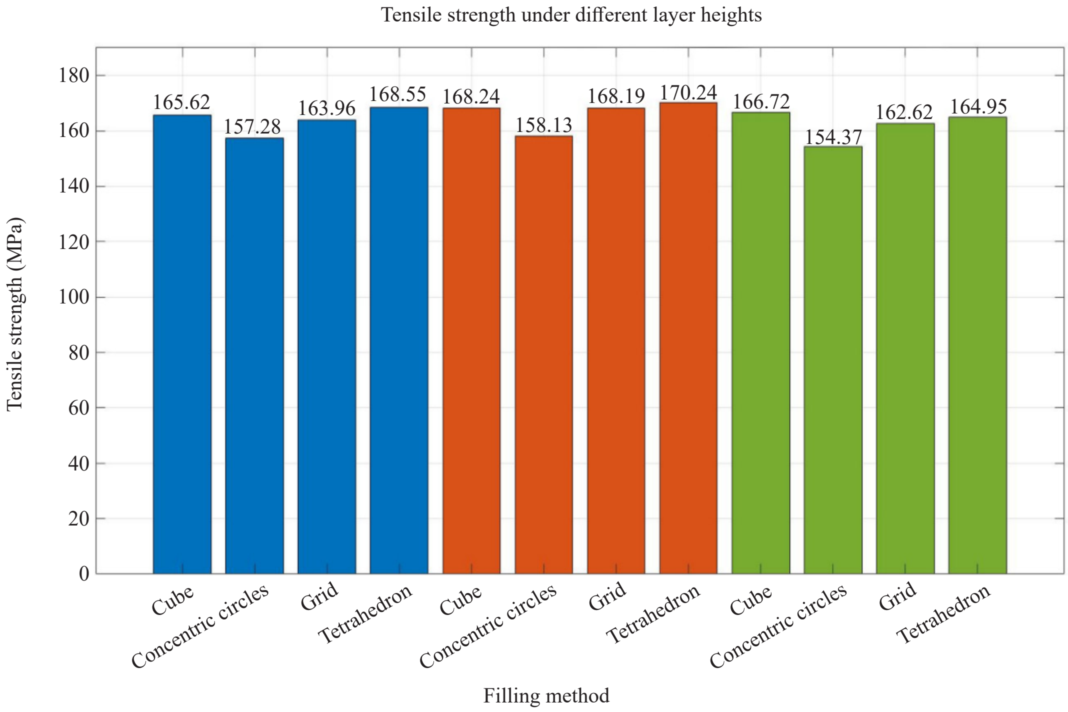

Figure 6. Tensile strength of different filling methods

Figure 6 shows the tensile strength of different PEEK samples. As can be seen from the histogram, the tensile strength of all PEEK samples exceeded 160 MPa except for the concentric circle filling method. When the filling method is concentric circle filling, the performance of the test piece is poor. At the same nozzle temperature, the platform temperature and the filling method of different filling methods have different degrees of PEEK wire bonding [11]. At the same time, the filling direction of different filling methods is different, and the tensile performance of the test piece is better when the filling direction is the same as the tensile direction. Additionally, complex filling methods effectively disperse external loads by optimizing material distribution and stress transfer paths, thereby enhancing properties such as tensile strength and flexural strength.

In this experiment, 12 sets of experiments were compared, and the most suitable filling method and printing parameters were selected by comparing their different tensile strengths in different filling methods (Table 2).

Table 2. Tensile strength of test pieces

Numbering	Floor height/mm	Platform temperature, °C	Filling method	Tensile strength/MPa
1	0.1	120	Cube	165.62
2	0.1	120	Concentric circles	157.28
3	0.1	120	Grid	163.96
4	0.1	120	Tetrahedron	168.55
5	0.2	120	Cube	168.24
6	0.2	120	Concentric circles	158.13
7	0.2	120	Grid	168.19
8	0.2	120	Tetrahedron	170.24
9	0.3	120	Cube	166.72
10	0.3	120	Concentric circles	154.37
11	0.3	120	Grid	162.62
12	0.3	120	Tetrahedron	164.95

The goal of this experiment is to optimize tensile strength, which is directly proportional to the performance of the part. When the tensile strength is greater, the part performs better. Therefore, the optimal combination of parameters is 0.2 mm layer height, 120 °C platform temperature, and the tetrahedral filling method, which provides printing parameters for subsequent heat treatment.

3.2 *Experimental preparation*

3.2.1 *Preparation of experimental materials*

The 3D printing material used in this paper is PEEK filament produced by Dongguan Hongkai Composite Materials Co., Ltd., with a diameter of 1.75 mm, a density of 1.3 g/cm^3, a glass temperature of 143 °C, and a melting temperature of 343 °C. The samples are mainly divided into mechanical property test samples, which are prepared by the FDM printing mechanism.

3.2.2 *Main instruments and equipment*

The specimens used in this experiment are prepared by the Y2020 PEEK 3D printing machine produced by Shenzhen Juying 3D Instrument and Equipment Co., Ltd.; the tensile performance test was carried out on the WDW-100D microcomputer-controlled electronic universal testing machine produced by Jinan Chuanbai Instrument Co., Ltd., which has a maximum tensile force of 100 kN. The equipment used in the heat treatment experiment is a muffle furnace produced by Naberherm Industrial Furnace Co., Ltd. in Germany.

3.3 *Effect of heat treatment on the tensile strength of the test piece*

PEEK is highly sensitive to temperature, and the crystallinity of printed samples in low-temperature environments will be relatively low, which can affect mechanical properties [12]. To improve its mechanical properties, it can be maintained above the glass temperature for a period of time through subsequent heat treatment, which can improve its crystallinity and eliminate internal residual stress, thereby improving the mechanical properties and making up for the defects of poor mechanical properties of printing and molding in low temperature environments [13].

3.3.1 *Experimental design of heat treatment*

According to the optimal printing parameters obtained from the tensile test, we heat treated the tensile specimen with a layer height of 0.2 mm, a platform temperature of 120 °C, and a tetrahedral filling method. The heat treatment method is divided into four groups, and the diagram shows the heat treatment parameter setting (Table 3).

Table 3. Heat treatment parameter settings

Numbering	Heat treatment parameter setting
1	Keep warm at room temperature to 60 °C for 2 h, take it out and air cool
2	Keep warm at room temperature to 100 °C for 2 h, take it out and air cool
3	Keep warm at room temperature to 140 °C for 2 h, take it out and air cool
4	Keep warm at room temperature to 180 °C for 2 h, take it out and air cool
5	Keep warm at room temperature to 220 °C for 2 h, take it out and air cool
6	Keep warm at room temperature to 260 °C for 2 h, take it out and air cool
7	Keep warm at room temperature to 300 °C for 2 h, take it out and air cool
8	Keep warm at room temperature to 340 °C for 2 h, take it out and air cool

The heat treatment modification temperature was designed according to the glass transition temperature (145 °C) and melting point (345 °C) of the matrix material PEEK. In the process of modification, the heating rate is 15 °C/min, after the temperature rises to 240 °C, the cooling rate is 5 °C/min, the insulation time is 120 minutes, and the specimen is air-cooled after the insulation is completed, and then the tensile test is carried out on the heat-treated specimen. Figure 7 shows the setting of heat treatment, Marten furnace temperature, and holding time.

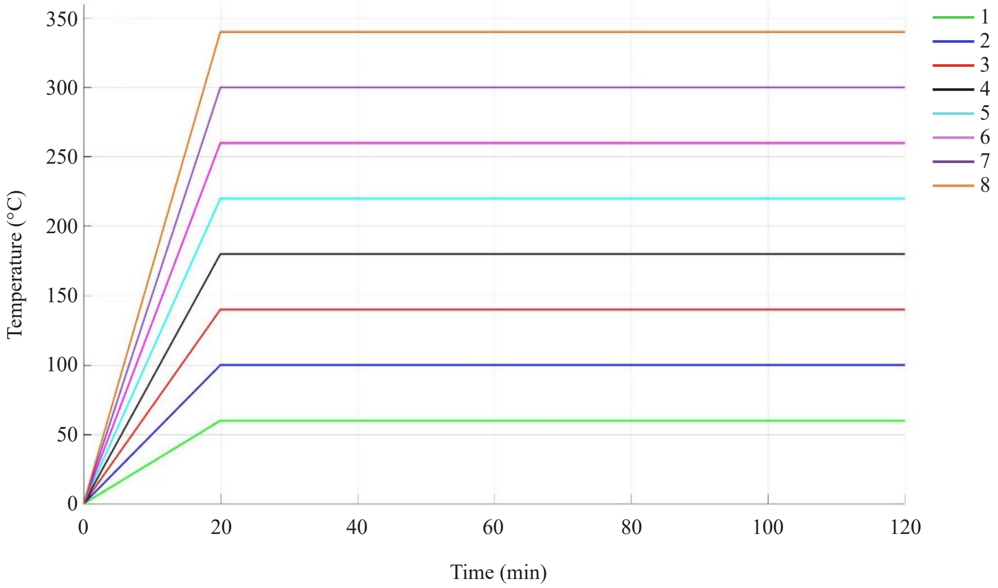

Figure 7. Heat treatment parameter settings

3.3.2 *Discussion of experimental results*

The tensile strength of the stretched part is 181.14 MPa when the insulation temperature is 340 °C, and the tensile strength of the stretched part without heat treatment is increased by 10.9 MPa, and the tensile strength is increased by 15.03%, as illustrated in Figure 8.

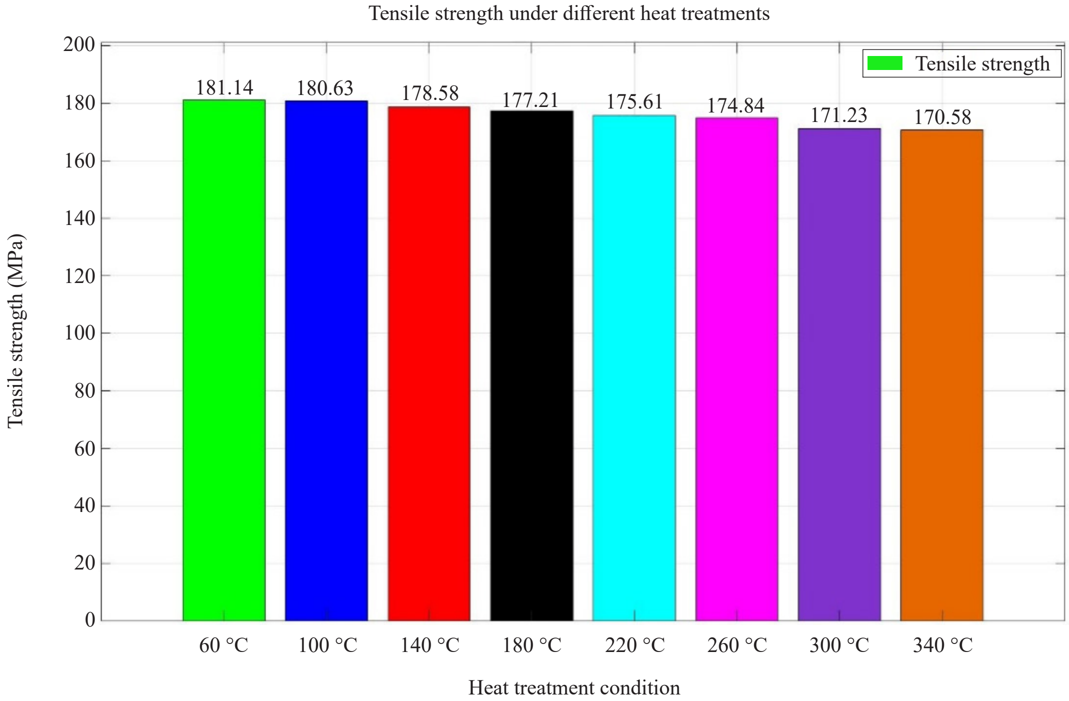

Figure 8. Tensile strength after heat treatment

According to the comparison of the tensile strength of the heat-treated specimens, it is found that PEEK material is more sensitive to insulation temperature, and when the temperature is higher than its vitrification temperature, the better the bonding degree of the test piece, the higher the tensile strength. The tensile strength is determined by combining heat treatment experiments with tensile experiments, which provides data support for subsequent simulations.

4. Experiments and simulations

4.1 *Simulation of the dynamics of the automobile suspension swing arm*

The front suspension system of automobiles is mainly composed of key components such as swing arms, steering knuckles, shock absorbers, springs, connecting rods, and body connection brackets [14]. During the driving process of the vehicle, the swing arm, as an important structure for load-bearing and guidance, is connected to the steering knuckle through the ball joint, and jointly controls the up and down movement of the wheels and the change of positioning angle with the body connection point. When the vehicle is steering and cornering, the suspension system adjusts the wheel attitude and shock cushioning through the linkage between the connecting rod and the shock absorber. In a typical MacPherson front suspension system, the lower swing arm is connected to the subframe and knuckle at both ends, and bushings or ball joints are usually set up in the middle to accommodate dynamic deformation and steering torque transmission.

The swing arm adopts 4 mounting points to fix and link with the body and knuckle, two of which form a flexible connection with the shock absorber/stabilizer bar. The up and down movement of the entire suspension is completed by the expansion and contraction of the shock absorber and the angle change of the stabilizer bar. The thickness of the swing arm is about 7 mm, and it is adopted QT540 cast iron material, which is made of low-density, high-strength, and has good fatigue resistance, which can meet the stress needs of high-speed driving and complex road conditions. As shown in the Table 4, some of the mechanical property parameters of the cast iron material are shown [15].

Table 4. Material properties of QT350-QT550 cast iron

Poisson's ratio	Density kg/m^3	Young's modulus G/Pa	Yield strength	Tensile strength
0.275	7.1	172	353	556

Referring to the actual operating conditions of the suspension system, six revolute joints were applied at the ball-joint connection, bushing connection, and stabilizer-bar connection locations of the lower control arm. A total of thirty-six fixed joints were applied in the connection region between the subframe and the lower control arm, while a motion joint was applied at the connection between the shock absorber and the linkage. By performing dynamic simulations of suspension motion during vehicle start-up, braking, and steering, the force variations experienced by the lower control arm under typical operating conditions were obtained.

To ensure the reliability and fidelity of the dynamic simulation results, the boundary conditions were further specified. The vehicle body reference coordinate system was fully constrained, and fixed joints were applied at the suspension-body connection points. An ideal spherical joint model was used between the lower control arm and the steering knuckle to allow three rotational degrees of freedom. The shock absorber was modeled as an extendable constraint with damping, parameterized according to a typical passenger-vehicle damping-velocity characteristic curve. A compliant hinge was introduced between the stabilizer-bar end and the lower control arm to represent the actual compliance of the bushing. A simplified tire model based on the Pacejka "Magic Formula" for longitudinal and lateral forces was adopted to reflect the realistic tire-road interaction forces during steering and braking. Dynamic simulations of suspension motion during vehicle start-up, braking, and steering were conducted to obtain the force variations on the lower control arm under representative operating conditions [16]. The specific driving maneuvers simulated included:

(1) Standard start-up condition: uniform acceleration from 0 to 1.2 m/s^2;

(2) Emergency braking condition: application of an instantaneous braking force corresponding to -4.5 m/s^2 deceleration;

(3) Steady-state steering condition: constant-speed driving at 50 km/h with a steering-wheel input rate of 5° per s to generate sustained lateral forces.

These maneuvers, defined with reference to standard vehicle-dynamics test cycles, effectively excite the characteristic longitudinal, lateral, and vertical combined loads of the suspension system, thereby capturing the complex loading state of the lower control arm under real-world conditions.

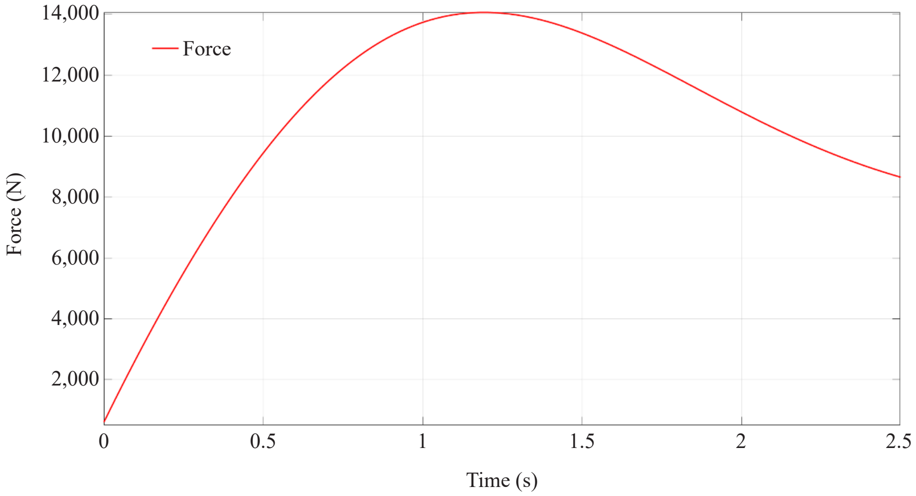

Figure 9. The force of the swing arm

The simulation results indicate that the lower control arm experiences a maximum load of 14,036.32 N during steering and cornering maneuvers, with a corresponding rotation angle of approximately 60°. These results clarify both the magnitude and direction of loading acting on the control arm under critical operating conditions, thereby providing essential boundary conditions for subsequent static analysis and topology optimization. Figures 9-11 illustrate the time-history curves of the forces, rotation angles, and velocities of the lower control arm during the vehicle start-up scenario.

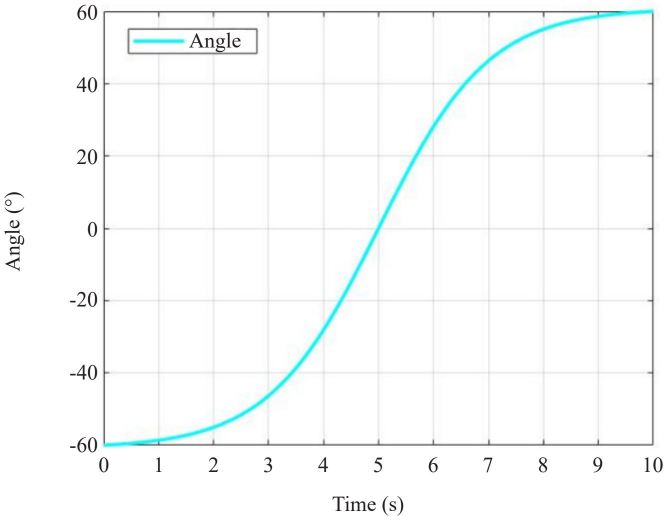

Figure 10. Movement angle of the swing arm

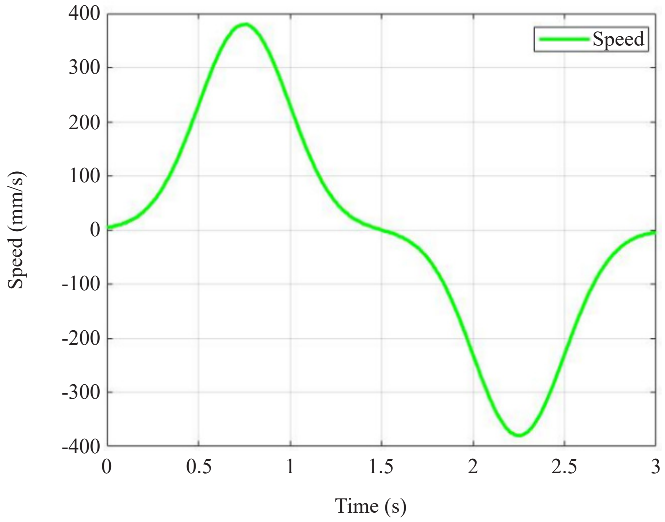

Figure 11. Movement speed of the swing arm

The force of the swing arm when the car starts is obtained by simulating the dynamics of the car start, and the maximum force of the swing arm is 14,036.32 N when the car starts, and the swing arm rotates clockwise by 60°. The magnitude and direction of the force on the swing arm during the static analysis are determined, which provides data for subsequent simulations.

4.2 *Static simulation of the automobile suspension swing arm opening and closing*

Compared with the QT550 cast iron commonly used in automotive suspension lower control arms, the maximum equivalent stress experienced by the control arm during typical driving and steering conditions remains well below the tensile strength of QT550. This indicates that the structure still possesses significant weight-reduction potential. Reducing the mass of the vehicle contributes to improved acceleration performance and handling stability. For chassis suspension systems in particular, decreasing unsprung mass can further enhance ride comfort and steering responsiveness [17]. To achieve additional lightweighting and performance optimization, replacing the conventional cast-iron lower control arm with the high-performance engineering polymer PEEK is considered a highly feasible solution. PEEK exhibits excellent specific strength and fatigue resistance [18]; its strength is comparable to, or even surpasses, that of certain cast irons, while its density is only about one-third that of cast iron. This allows for substantial component weight reduction while maintaining overall suspension stiffness and reliability. Compared with conventional metallic materials, PEEK exhibits superior impact resistance and excellent chemical stability, enabling it to withstand exposure to oil, humidity, and certain corrosive environments. During processing, complex geometries can be realized through additive manufacturing techniques such as FDM or other 3D printing methods, thereby enhancing assembly compatibility and design flexibility. Furthermore, its low coefficient of thermal expansion and favorable long-term creep resistance allow it to maintain high dimensional stability and reliability under elevated temperatures or cyclic loading conditions. These attributes collectively reinforce the overall competitiveness of PEEK for applications in automotive suspension systems. Representative mechanical properties of PEEK are shown in Table 5. Based on these characteristics, integrating PEEK into the lower control arm design has the potential to achieve significant lightweighting without compromising mechanical performance, thereby offering a new materials-based pathway for chassis structural design.

Table 5. Performance parameters of PEEK materials

Poisson's ratio	Density kg/m^3	Young's modulus G/Pa	Yield strength	Tensile strength
0.2	1.3	3,738	79.25	83.38

The swing arm is modeled using SolidWorks software pairs. The STEP format model and PEEK material performance parameters of the 3D model of the swing arm, modeled using SolidWorks software, were imported into Ansys for static simulation [19]. The finite element meshing of the swing arm is shown in the Figure 12.

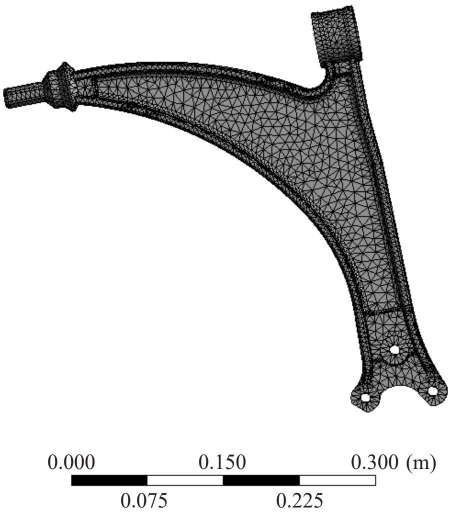

Figure 12. Finite element grid division of automobile suspension swing arm structure

The lower surface of the swing arm structure is fixed with the wheel knuckle, and the left mounting hole is fixed with the body subframe. In the normal stationary state of the car, due to the action of the wheel and the vehicle's own weight, the swing arm bears the vertical downward gravity load and part of the vertical force from the wheel. When the vehicle is in a working condition, such as turning or crossing obstacles, the swing arm will bear the lateral force at a certain angle to the outside. When the vehicle encounters an emergency situation and needs emergency braking, the swing arm will still be subjected to the braking force from the body. Here, the influence of the force on the swing arm structure under the static state of the vehicle and the operating conditions of the vehicle is calculated [20].

Before extracting the load at the three connection points of the swing arm, the tire grip force under each working condition under three typical working conditions is calculated according to the empirical formula, namely the maximum vertical, maximum lateral force, and maximum braking force under the working conditions.

(1) Maximum vertical force condition.

When a car is driving in a straight line on the road, the maximum vertical force at the point of contact between the wheels and the road surface is:

$$F_{vm2} = K_2 F_{v0} \tag{6}$$

In the formula, F_{v0} is determined by the static load when a single front wheel is fully loaded, and the full load mass of the front axle $m_1 = 1{,}145.8$ kg; $F_{v0} = 1{,}145.8 \times 9.8/2 = 5{,}614.53$ N; K_2 is the dynamic load coefficient of static strength [21], take $K_2 = 2.5$; the maximum vertical load $F_{vm2} = 14{,}032.36$ N.

(2) Maximum lateral force condition.

Normally, the maximum lateral force working condition should choose the state when turning, but the direction of the bending moment caused by the lateral force and the vertical force during turning is opposite, canceling each other out, resulting in a decrease in the synthetic bending moment. The road measurement results show that the stress caused by the lateral force of ordinary cars driving in a straight line is higher than that of turning, so the maximum lateral force condition is studied in a straight line. When a car is driving in a straight line on the road, under the maximum lateral force condition, it is subjected to the maximum lateral force and vertical load, and the maximum lateral force will not appear at the same time as the maximum vertical force. The lateral force F_{Lm} and vertical force F_{vm} are calculated as follows:

$$F_{Lm2} = \mu_{F2} F_{v0} 0.7 \times 5,614.53 \text{ N} = 4,032.58 \text{ N}$$

μ_{F2} is the lateral force coefficient used for static strength calculation, take 0.7;

$$F_{vm} = K_1 F_{v0} 1.55 \times 5,614.53 \text{ N} = 8,702.5 \text{ N}$$

K_1 the dynamic load coefficient of vertical load is calculated for durability, which is 1.55.

(3) Maximum braking force working condition.

When the car brakes urgently at low speed, the longitudinal adhesion coefficient between the front wheel and the road surface $\mu_B = 1.5$, and the maximum ground braking force of the front axle is: $F_B = 1.5$, $F_{v0} = 8{,}446.52$ N. The obtained tire grounding force is input into the suspension dynamic model, and the load at the connection point of the swing arm is obtained in the simulation results. As an important component on the suspension of the automobile, the swing arm must be analyzed for strength, analyze the value and position of the maximum stress it bears, see if it meets the performance requirements, whether the fracture failure phenomenon occurs, and provide constraints for subsequent optimization. According to the loads under the three extracted conditions, the boundary is defined, and the strength analysis of the swing arm is carried out by the inertia release method to prepare for subsequent optimization (Table 6).

Table 6. Stress on the swing arm

Working conditions	Direction of force	The amount of force exerted
1	Maximum vertical force	14,032.36 N
2	Maximum lateral force	4,032.58 N
3	Maximum braking force	8,446.52 N

It is known from the Figure 13a that the maximum equivalent stress of the swing arm in working condition 1 is 104.37 Mpa, the maximum stress is at the fixed connection between the swing arm and the body, the maximum equivalent stress of the swing arm in working condition 2 is 93.93 Mpa (Figure 13b), the maximum stress is at the junction of the outside of the swing arm, and the maximum stress of the swing arm in working condition 3 is 99.06 MPa (Figure 13c). The greatest stress is at the junction between the swing arm and the body. Compared with the QT350-QT550 cast iron material of the swing arm, the yield strength and tensile strength of PEEK material can meet the stress load during the movement of the car, and reduce the overall mass of the car when the strength meets the normal operation of the car. At the same time, PEEK material has better anti-vibration performance, which meets the vibration load of the suspension system when the car is driving, when the car starts and stops, so that the car suspension swing arm has a longer service life [22].

Figure 14 shows the overall displacement diagram of the swing arm under extreme working conditions. The analysis shows that the outer point of the swing arm has a large displacement (0.974 mm) under the maximum vertical force condition. The maximum displacement under the maximum lateral force condition (0.731 mm) is smaller than that under the vertical force condition. Under the maximum braking force condition, the external fulcrum displacement of the swing arm is large (0.487 mm). Under the above limit supply conditions, the displacement of the swing arm exceeds the allowable range and meets the performance requirements.

Based on the suspension dynamics simulation of the force size and direction of the swing arm, the stress concentration position and the equivalent stress size under different working conditions are obtained to prepare for the subsequent topology optimization design.

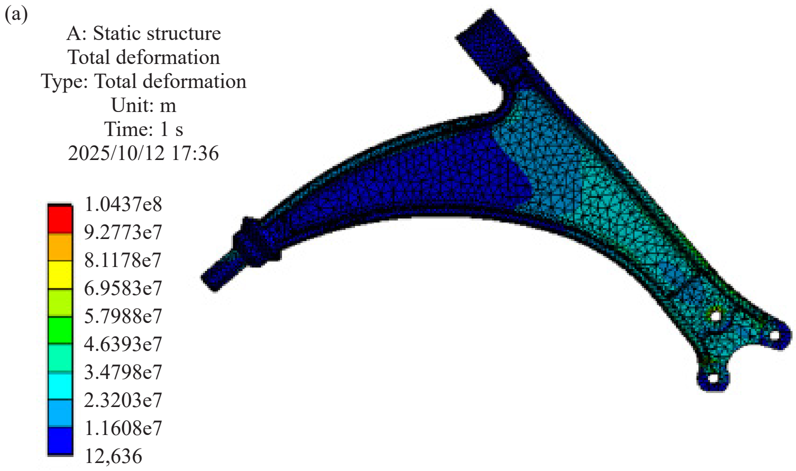

Maximum vertical force condition

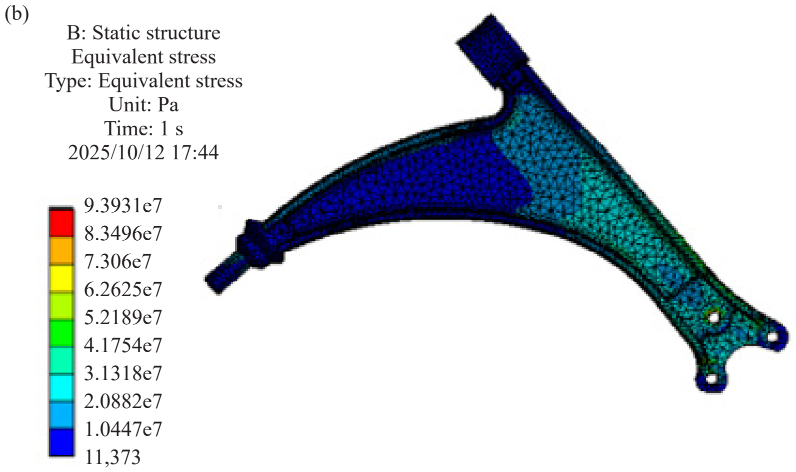

Maximum lateral force condition

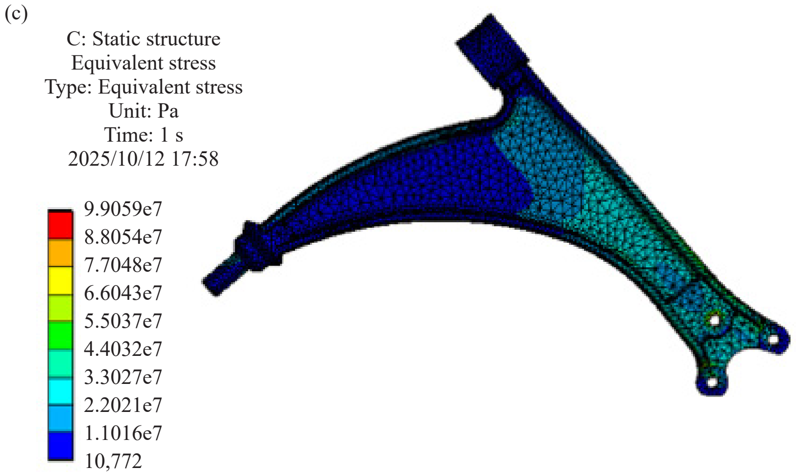

Maximum braking force condition

Figure 13. Stress cloud diagram of the swing arm under three working conditions

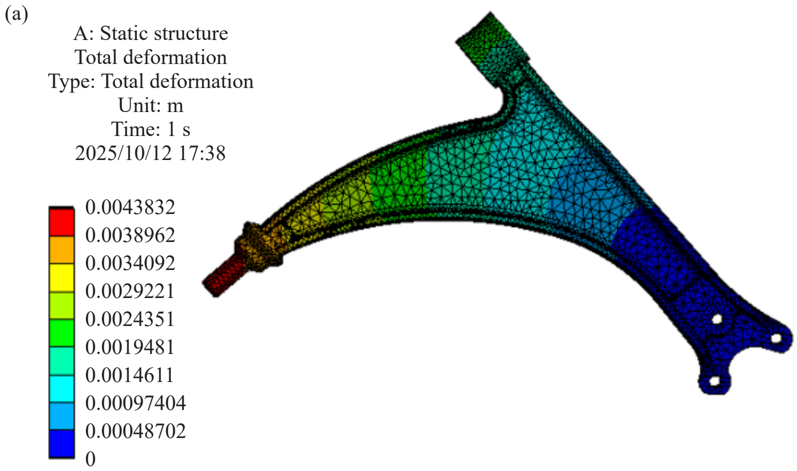

Maximum vertical force condition

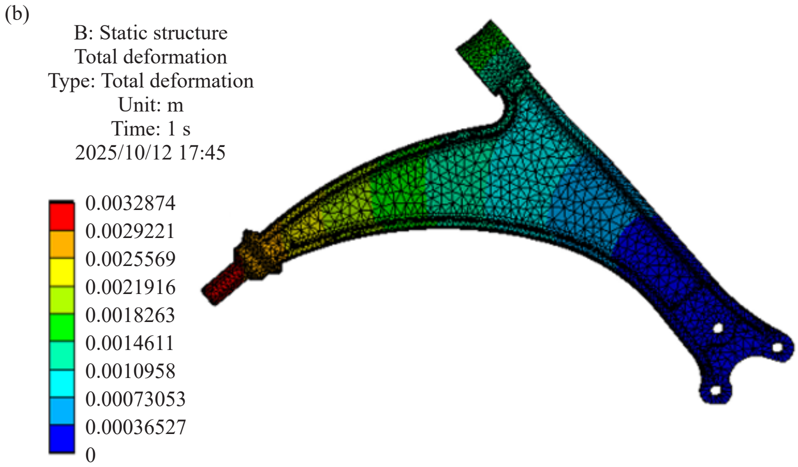

Maximum lateral force condition

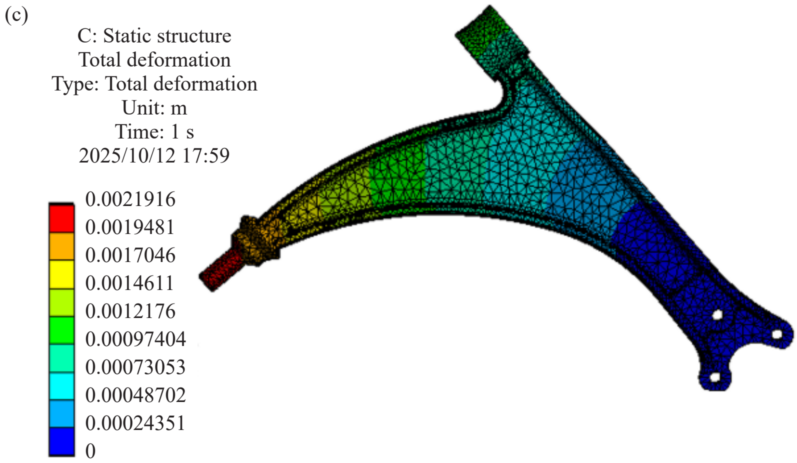

Maximum braking force condition

Figure 14. Cloud diagram of the displacement of the swing arm under three working conditions

4.3 *Topology optimization of the swing arm*

4.3.1 *Topology optimization parameter setting*

Common methods of topology optimization include the homogenization method, the progressive structure optimization method, and the variable density method. In this analysis, the variable density method is used to optimize the topology of the support structure. The variable density method assumes that the material density is variable, and the relative density of the structural unit varies continuously between 0 and 1 through the density penalty method, so as to establish the interpolation relationship between the relative density of the unit and the material properties, and transform the structural topology optimization problem into a material optimization problem. The variable density topology optimization mathematical model with the minimum structural flexibility (maximum stiffness) as the constraint is as follows:

$$\text{find } \rho_i \ (i = 1, 2, \cdots, n) \tag{7}$$

$$\min_{i \in j \in p} \max C_j \tag{8}$$

$$\text{s.t. } \frac{\sum_{i=1}^{n} \rho_i \rho_0 V_{oi}}{m_0} \le a \tag{9}$$

$$0 \le \rho_i \le 1 \tag{10}$$

where ρ_i is the relative density of the element i; C_j is the total flexibility of the structure; p is the total number of working conditions; ρ_0 is the original density of the unit; V_{oi} is the volume of the element i; m_0 is the total mass of the structure when the original density is taken for all elements; a is the mass retention percentage [23].

4.3.2 *Topology optimization model*

Using Ansys software to perform static analysis and topology optimization, the optimization target is the support structure as a whole, the response constraints are set to mass and intensity, and the retained mass is set to 40%.

In the optimization process, the tensile strength, yield limit, and the performance enhancement of PEEK after heat treatment—derived in Section 1—were incorporated into the model through the implementation of strength-based safety constraints [24]. When applying the *Strength Constraint* in Ansys, the allowable design stress was defined as:

$$\sigma_{\text{allow}} = \frac{\sigma_{\text{PEEK}}}{\gamma} \tag{11}$$

where the safety factor γ was set to 1.5 to ensure sufficient redundancy for PEEK under dynamic loading, impact conditions, and potential manufacturing imperfections. This safety factor was consistently applied across all three representative operating conditions—vertical loading, lateral loading, and braking load cases—to guarantee that the optimized topology would not experience yielding or fatigue-related failure. The optimization area and load application settings of the swing arm are shown in Figure 15.

To ensure the stability and convergence of the topology optimization process, the following convergence control parameters were configured in Ansys/OptiStruct [25]:

(1) Maximum number of iterations: 150. This allows sufficient exploration of the design space and prevents premature termination of the optimization process.

(2) Objective function convergence threshold: 1×10^{-3}. Convergence is assumed when the change in the objective function between two consecutive iterations is less than 0.1%.

(3) Density change tolerance: 1×10^{-2}. The density-based convergence criterion is satisfied when the average

change in the elemental relative density is below 1%.

(4) Filter radius: 1.5-2.0 mm. This is used to suppress checkerboard patterns and mitigate numerical instabilities.

These convergence criteria and filtering strategies collectively ensure the geometric stability and manufacturability of the optimized topology, while preventing local oscillations and non-physical density distributions commonly observed in unconstrained optimization processes.

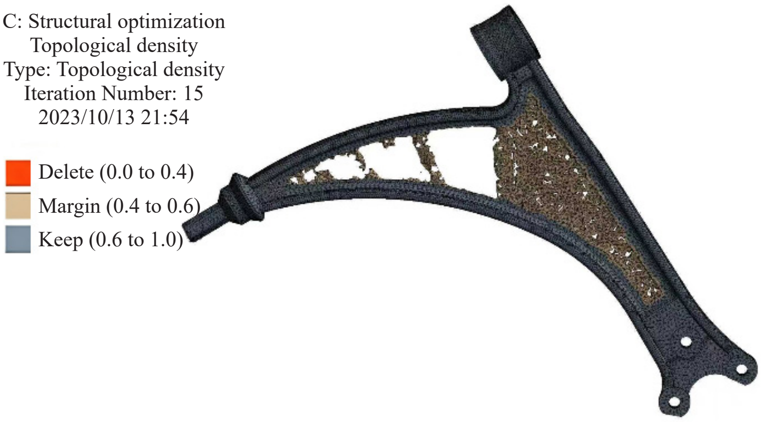

Figure 15. Topology optimization settings of the swing arm

4.3.3 *Topology optimization shape control*

Ansys provides designers with two methods of shape control: draft control and symmetry control. Draft control includes one-way draft, two-way draft, radial, extrusion and suspension. By setting up shape control, it is effective to ensure that the model has good machinability after the design space is optimized. Therefore, shape control is a critical step before topology optimization. Different shape control settings will affect the results of topology optimization, so the shape control setting is an exploratory process in the optimization process. For curved supports, the Structural Optimization Module sets the initial shape control to bidirectional draft and applies the shape control to the plane of symmetry (YZ plane) [26]. In the process of topology optimization, it is necessary to set the topology optimization parameters for the model with the load conditions, design space, and shape control settings. Once the topology is optimized, the Poly Non-Uniform Rational B-Splines (NURBS) auto-fitting feature included in the Ansys software creates 3D solids, and the Optistruct solver verifies that the materials in the optimization results meet the requirements. To ensure that the stress distribution satisfies the optimization requirements after incorporating the safety factor, a strength verification is performed on the Poly NURBS solid model. The optimized geometric model is loaded under the same three representative operating conditions. If any local stress exceeds the allowable limit ($\sigma > \sigma_{\text{allow}}$) during the verification stage, the topology is locally modified by adjusting wall thickness, followed by re-iteration of the optimization process. This procedure ensures that the final structure complies with the material strength constraints.

4.3.4 *Optimize process analysis*

Figure 16 shows the optimized stress distribution cloud of the swing arm, and Figure 17 shows its overall displacement distribution. By reducing the local thickness in the structure and setting a weight reduction hole in the middle, the stress of the swing arm is mainly concentrated between the rear fulcrum and the outer fulcrum under the maximum vertical load condition, and the maximum stress value reaches 168.11 MPa, corresponding to a maximum deformation of 3.36 mm. In the maximum lateral load condition, the stress concentration area is located at the stiffener between the outer fulcrum and the rear fulcrum, with a maximum stress of 144.94 MPa and a maximum displacement of 3.07 mm. Under the maximum braking force condition, there is no obvious stress concentration area in the overall structure, and the maximum displacement is only 1.85 mm. The results of the analysis of the ultimate working conditions show that there is no stress concentration phenomenon around the punching area, and the stress level and displacement are within the allowable range. The "allowable limit" mentioned above corresponds to the material strength constraint after incorporating the safety factor. That is, the maximum equivalent stress under all loading conditions satisfies $\sigma_{\text{max}} < \sigma_{\text{allow}} = \sigma_{\text{PEEK}}/1.5$. Verification results indicate that the optimized geometry retains a sufficient safety margin even after applying the safety factor. This shows that after the lightweight design, the swing arm still has good strength and stiffness characteristics, which can meet the requirements of use under actual working conditions.

Based on three typical load cases—specifically, maximum vertical load (14,032.36 N), maximum lateral load (4,032.58 N), and maximum braking load (8,446.52 N)—the topology optimization employs a multi-condition combination approach to achieve a unified structural solution, with the weighted sum of compliances serving as the core methodology. First, static analyses are conducted separately under the three load cases to determine the structural compliances (C_1, C_2, C_3) of the lower control arm in each scenario. The vertical load reflects the stiffness requirement under straight-line driving and obstacle-crossing conditions, the lateral load characterizes the transverse stiffness during steering and steady-state operation, and the braking load corresponds to extreme safety conditions such as emergency braking. Weighting factors (w_1, w_2, w_3) are then assigned based on the importance and risk levels of these load cases during vehicle operation, forming a combined objective function $C = w_1C_1 + w_2C_2 + w_3C_3$. Throughout the optimization iterations in Ansys/OptiStruct, the weighted compliance is treated as the unified objective, ensuring that material distribution is constrained by all three load cases simultaneously. This approach mitigates the risk of insufficient stiffness under lateral or braking scenarios, which may arise from optimization targeting only the maximum vertical load. Through this multi-condition combination strategy, the optimized lower control arm satisfies both strength and displacement requirements under the three extreme loading conditions, achieving a lightweight structural design that provides optimal overall performance in real-world service environments. Specific calculations are as follows. The weighting coefficients are determined via a load amplitude normalization approach, i.e.,

$$w_i = \frac{F_i}{F_1 + F_2 + F_3} \tag{12}$$

The total load is

$$F_{\text{sum}} = 14,032.36 + 4,032.58 + 8,446.52 = 26,511.46 \text{ N}$$

Then the weights of the three working conditions are respectively

$$w_1 = \frac{14,032.36}{26,511.46} \approx 0.5$$

$$w_2 = \frac{4,032.58}{26,511.46} \approx 0.15$$

$$w_3 = \frac{8,446.52}{26,511.46} \approx 0.32$$

In the finite element analysis, the structural compliance under the three different working conditions is denoted as C_1, C_2, and C_3 respectively. Then, the comprehensive objective function of the topology optimization is

$$C = 0.53\ C_1 + 0.15\ C_2 + 0.32\ C_3 \tag{13}$$

It indicates that the maximum vertical load condition during the optimization process has the greatest impact on the material distribution, followed by the braking force condition, while the lateral load has the smallest impact. By incorporating the above weights into the topology optimization model, it is possible to ensure that the optimized lower arm has reasonable stiffness under the three extreme conditions, achieving a multi-condition comprehensive optimal design for real road load conditions.

The swing arm was analyzed in Ansys using free-mode analysis [27]. The natural frequency of the 1st to 6th order is simulated, see Table 7, and the natural frequency and mode shape of the optimized swing arm show that the natural frequency of the first order is higher than the excitation caused by the imbalance between the wheel and the drive shaft and the excitation caused by the bumps and convex of the road surface, and the natural frequency of the second order is also much higher than the frequency of the engine of 25~28.3 Hz, so the optimized swing arm will not resonate with other parts, ensuring the dynamic characteristics of the swing arm.

Table 7. Stress on the swing arm

Modal order	Natural frequency/Hz
1	36.52
2	390.34
3	452.85
4	660.21

Table 7 presents the first four natural frequencies of the topology-optimized lower control arm, among which the first-order natural frequency is 36.52 Hz, and the second-order natural frequency reaches 390.34 Hz, while the remaining higher-order frequencies are all above 450 Hz. For automotive suspension systems, the dominant vibration frequencies induced by road roughness and tire imbalance are generally concentrated in the range of 1-20 Hz, whereas the primary excitation frequencies associated with the engine and powertrain typically lie within 25-30 Hz. If the natural frequencies of the lower control arm overlap with these excitation bands, structural resonance is likely to occur, leading to a significant amplification of vibration amplitude and consequently resulting in noise, joint loosening, or even fatigue damage.

The modal analysis results indicate that the first natural frequency of the optimized lower control arm (36.52 Hz) is distinctly higher than the dominant excitation ranges of both engine and road-induced vibrations, while the second and higher modes are far removed from the operational frequency spectrum of the vehicle. This demonstrates that, under normal driving and typical operating conditions, the lower control arm is unlikely to experience frequency coincidence with excitations originating from the tires, engine, or road surface, thereby effectively avoiding structural resonance from a dynamic perspective. Compared with conventional cast-iron designs, which often suffer from relatively low first-order natural frequencies, the topology-optimized structure maintains a high global stiffness despite significant mass reduction, leading to an overall upward shift of the natural frequency spectrum and thus markedly enhancing its vibration resistance.

Therefore, the modal results listed in Table 7 not only confirm the feasibility of the optimized structure in terms of static strength and stiffness but also substantiate its superior vibration performance in the frequency domain. By deliberately separating the critical natural frequencies from the major excitation bands of the vehicle, the proposed lightweight design of the lower control arm effectively mitigates resonance risks while satisfying strength requirements, thereby providing solid support for improving the ride comfort and durability of the suspension system.

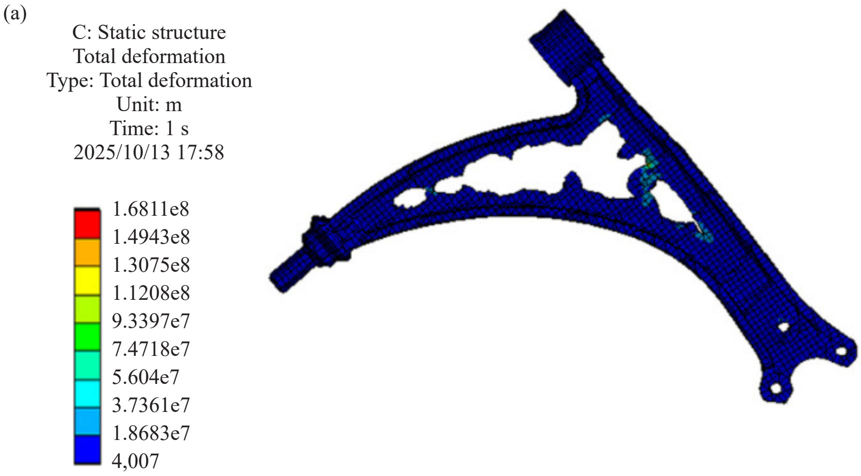

Maximum vertical force condition

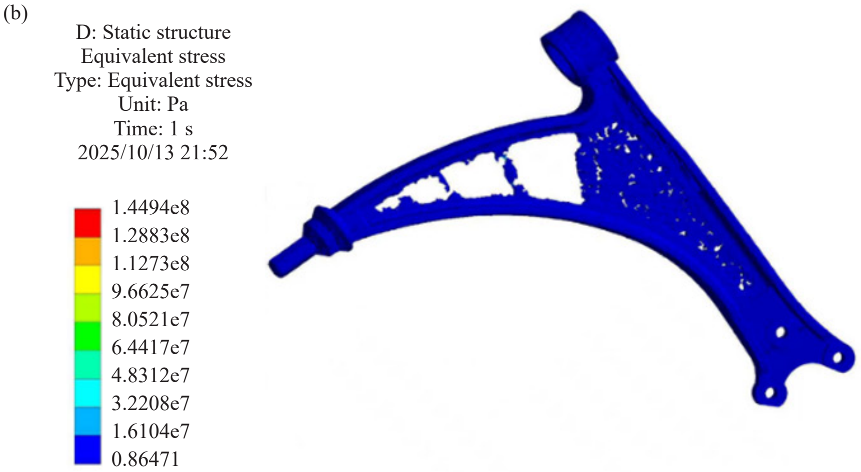

Maximum lateral force condition

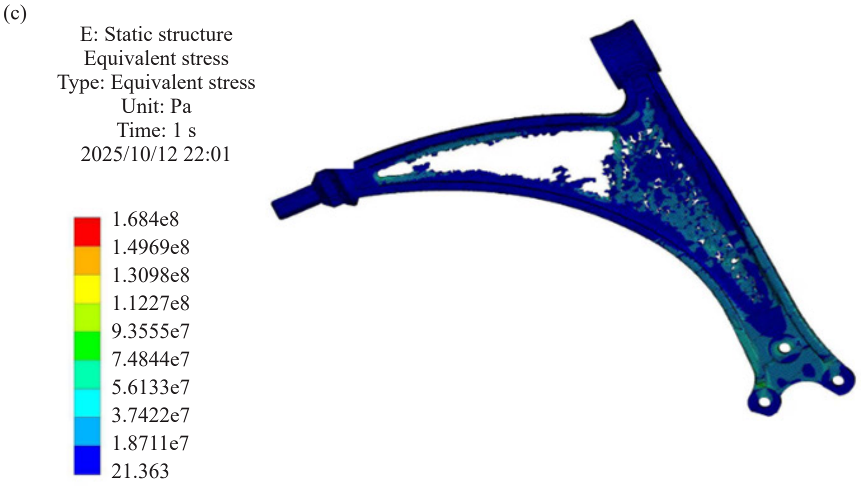

Maximum braking force condition

Figure 16. Cloud diagram of stress distribution of the swing arm after optimization

(a)

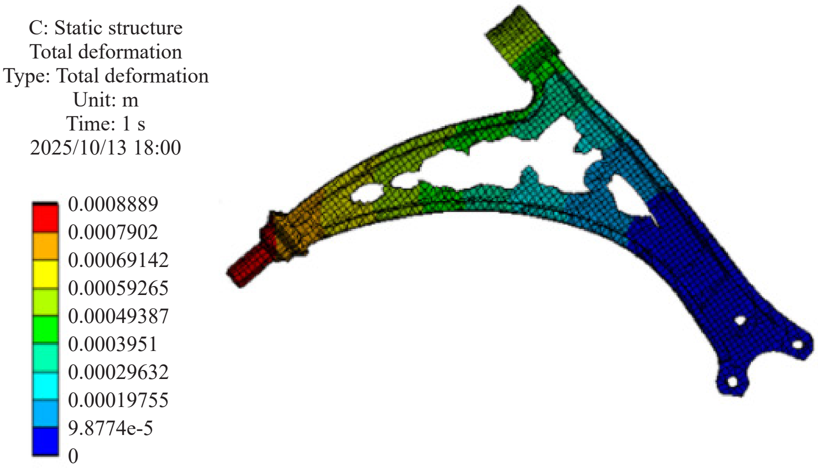

Maximum vertical force condition

(b)

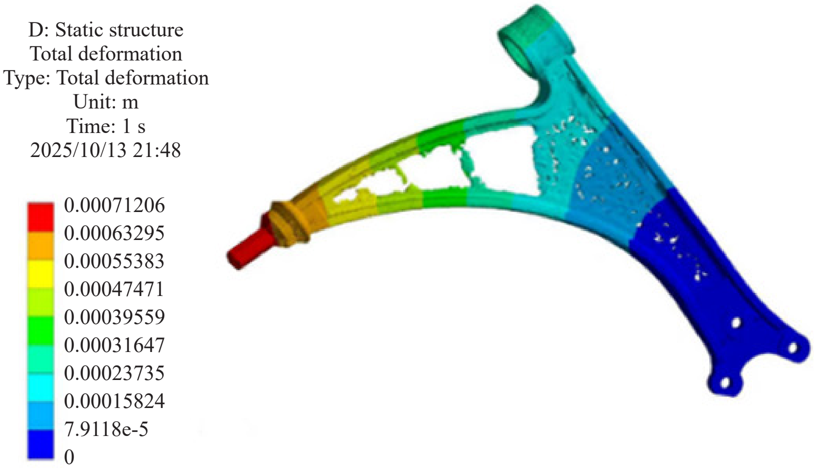

Maximum lateral force condition

(c)

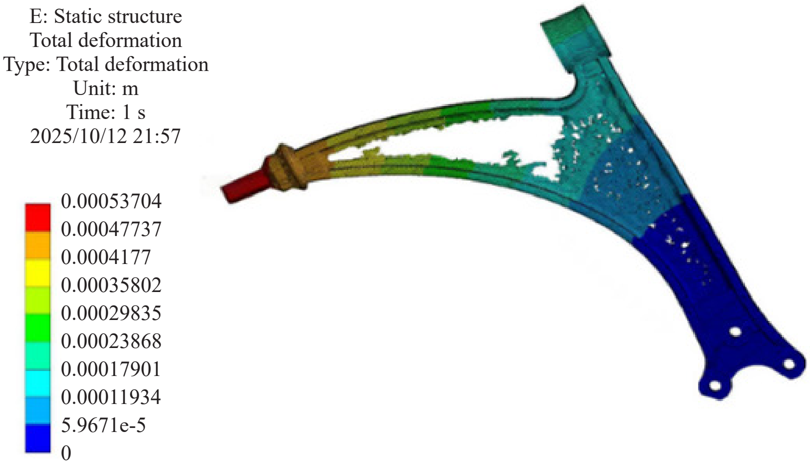

Maximum braking force condition

Figure 17. Displacement diagram of the swing arm after optimization

5. Discussion and analysis

This study presents a novel application of PEEK in the design of automotive suspension lower control arms. Initially, multibody dynamics simulations of the vehicle suspension system under normal driving conditions were conducted to obtain the forces, displacements, and velocities of the lower control arm, followed by an analysis of the forces during the arm's opening and closing motion. Static structural analysis using Ansys was then performed to determine the equivalent stresses and stress concentration regions under operational conditions. Subsequently, structural reconstruction was carried out to reduce local stress concentrations, and the original cast iron material was replaced with the lighter PEEK. Although the final topology-optimized components were not actually fabricated using FDM, overhanging sections were treated with partial adhesion or removal strategies to satisfy potential printing requirements.

Specifically, local regions with large overhang angles generated by topology optimization, typically exceeding 45°, are prone to collapse or poor interlayer bonding during FDM fabrication. For such regions, removable support structures can be enabled at the slicing stage, where support pillars or lattice-type supports are automatically generated beneath the overhanging surfaces to provide sufficient mechanical backing for the molten PEEK material during deposition. In addition, for slender cantilever features located in non-critical load-bearing areas, geometric reconstruction can be applied by introducing filleted transitions or thin connecting ribs, so that the features exhibit a "self-supporting" configuration along the printing direction, thereby reducing the dependence on external supports.

Furthermore, for extremely fine holes or fully enclosed internal cavities resulting from topology optimization, local removal or simplification can be performed without compromising the overall mechanical performance, such as eliminating unnecessary micro-voids or slightly increasing the local wall thickness to comply with the minimum feature size requirements of the FDM process. This "topology-to-manufacturability reconstruction" strategy enables the optimized lower control arm to retain its lightweight advantage while satisfying the technological constraints of PEEK FDM fabrication, including overhang angle limits, minimum wall thickness, and support removability, thus providing a feasible pathway for subsequent physical manufacturing.

Compared with mainstream metallic lower control arm development workflows, the core distinction of this study lies in the early integration of additive manufacturing feasibility during the structural design stage, rather than implementing secondary compromise designs under metal manufacturing constraints. By combining material substitution with topology optimization, this approach achieves lightweighting while overcoming the traditional limitations of "fixed material and structure-only optimization". The study further advances topology optimization based on load cases obtained from multibody dynamics simulations, avoiding the conventional approach of optimizing solely under a single static load, thereby producing results that better reflect actual service conditions.

Despite demonstrating the potential advantages of PEEK in suspension lower control arm design, the overall design methodology still differs from mainstream metallic workflows [28]. This study relies primarily on numerical simulations without validation through physical printed prototypes, leaving critical performance metrics—such as fatigue life, corrosion resistance, environmental adaptability, and long-term creep behavior—unverified under realistic operating conditions. Although topology optimization achieved substantial weight reduction, the increase in maximum stress suggests that some local regions may be over-optimized and structurally weakened, which contrasts with traditional metallic lower control arm designs that emphasize safety margins. Furthermore, the analysis of interlayer bonding, heat-affected zones during printing, and manufacturing consistency of PEEK remains insufficient, preventing the establishment of a systematic lightweight polymer suspension component design methodology. These limitations currently restrict the direct substitution of PEEK for conventional metallic components.

6. Conclusion

6.1 *Experiment conclusion*

The overall flowchart of this study is shown in Figure 18. The lower control arm was subjected to topology optimization using Ansys software, with the design process illustrated in Figure 19. It should be noted that the current experimental validation is based solely on numerical simulations. The main conclusions drawn from the analysis are as follows:

(1) The effects of FDM-based filling strategies and heat treatment methods were investigated. By comparing the tensile properties of specimens prepared under different parameters, the optimal printing parameters were determined. The best-performing specimen was printed with a layer height of 0.2 mm, a platform temperature of 120 °C, a nozzle temperature of 340 °C, and a tetrahedral filling pattern, achieving a tensile strength of 170.24 MPa. The optimal heat treatment conditions were identified as 340 °C with a holding time of 2 hours. Unlike metallic materials, the mechanical performance of FDM-fabricated PEEK is highly dependent on crystallinity, interlayer bonding strength, and the infill path, making the optimization of printing parameters a critical factor for structural reliability [29]. This study provides a systematic comparison of printing process parameters, revealing the causal relationship between microstructural optimization and macroscopic performance enhancement, which is a notable difference from traditional metallic component development.

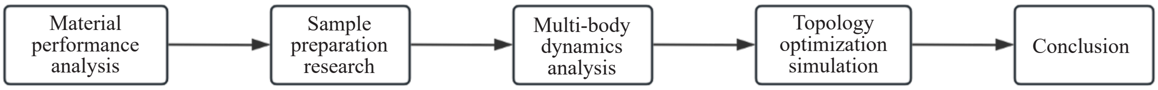

Figure 18. Overall visualization flowchart

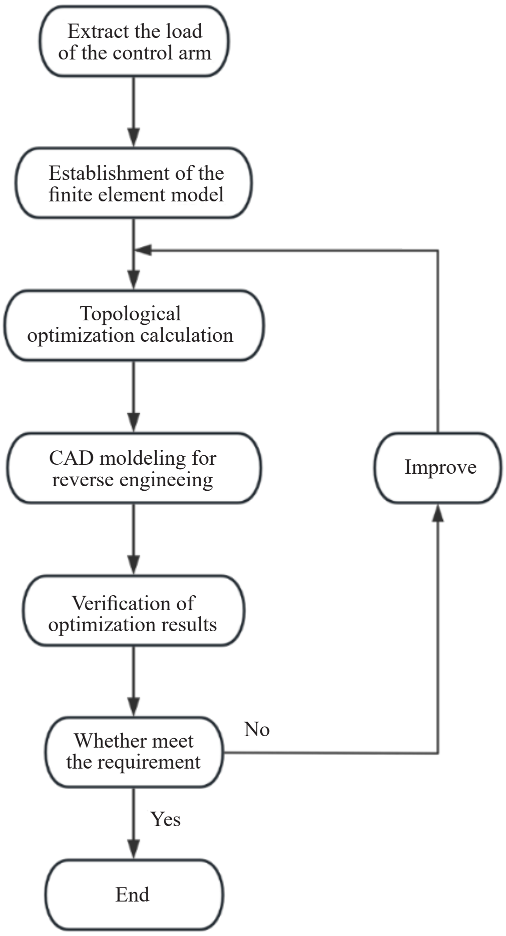

Figure 19. Flow chart of the overall structure of topology optimization

(2) Subsequently, a multi-body dynamics simulation of the automotive suspension system was conducted to obtain the force and displacement histories of the lower control arm during the opening of the vehicle door. Three different loading conditions were analyzed, and the corresponding force magnitudes and directions were determined. Static structural analyses were then performed in Ansys to obtain the equivalent stress distributions under each condition, as shown in Figure 20, with maximum stresses of 104.37 MPa and 168.11 MPa, 93.93 MPa and 144.94 MPa, and 99.06 MPa and 168.4 MPa, respectively. The maximum deformations under the different conditions are illustrated in Figure 21, with values of 0.974 mm and 3.36 mm, 0.731 mm and 3.07 mm, and 0.487 mm and 1.85 mm. This multi-condition analysis addresses the limitations of existing studies that typically optimize structures based on a single extreme scenario, making the optimization results more representative of real-world road excitations and multi-directional load combinations, thereby enhancing the engineering applicability of the topology optimization scheme.

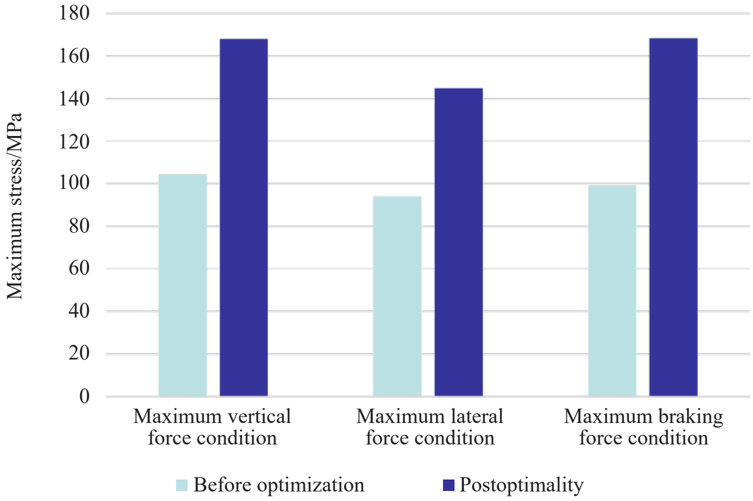

Figure 20. Comparison diagram of the maximum stress of the optimized front and rear swing arms

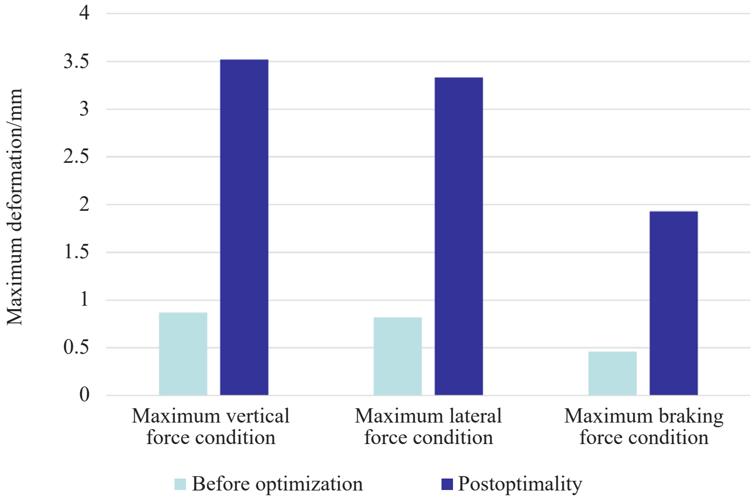

Figure 21. Comparison diagram of the maximum deformation variable of the optimized front and rear swing arms

(3) Based on the magnitude and direction of the forces obtained from static simulations, topology optimization of the lower control arm was performed using Inspire software. After optimization, the maximum equivalent stress

increased to 168.4 MPa, which is 69.34 MPa higher than the original design. The mass of the optimized lower control arm was reduced from 7.68 kg to 4.64 kg, achieving a 39.62% reduction. Furthermore, replacing the original cast iron material with PEEK further decreased the mass by 49.05%, accomplishing the goal of lightweight design. It should be noted that the significant reduction in mass not only decreases the unsprung mass but also directly affects the dynamic response of the entire suspension system. Lower unsprung mass typically improves tire-road contact under excitations, enhances suspension responsiveness, and increases energy absorption efficiency, thereby improving both vehicle handling stability and ride comfort. The observed increase in stress after topology optimization is primarily due to the algorithm's tendency to minimize compliance and remove unnecessary material, which concentrates load paths and results in higher local stresses. Although the stress levels remain within the strength limits of PEEK, this indicates that further assessment of safety factors, fatigue life, and creep performance is necessary. Unlike metallic materials, the long-term creep behavior of PEEK significantly influences the reliability of the optimized design, which remains a current limitation of this study.

6.2 *Future development trends*

Future research should build upon the current work by further refining the experimental framework. This includes performing FDM printing, heat treatment, and actual loading tests on topology-optimized lower control arms to comprehensively validate their mechanical performance and durability. Meanwhile, the adoption of multi-objective topology optimization algorithms is recommended, integrating factors such as mass, strength, fatigue life, and manufacturability into a unified framework to enhance the engineering applicability of the optimized structures.

In terms of materials, further exploration of Continuous Fiber-reinforced PEEK (CF-PEEK) or hybrid printing techniques could improve the strength and stiffness of critical load-bearing regions. Regarding process technology, establishing a more complete process window—including printing temperature, scanning path, infill strategy, and post-processing methods—would facilitate the development of a stable manufacturing workflow for PEEK-based suspension components [30].

With the continued advancement of lightweight design concepts, additive manufacturing technologies, and high-performance polymer materials, PEEK-based automotive suspension structures are expected to gradually transition from theoretical research to practical engineering applications, providing a novel technological pathway for vehicle weight reduction in the future.

Conflict of interest

The authors declare that they have no known competing financial interests or personal relationships that could have appeared to influence the work reported in this paper.

References

[1] R. Lin, X. Zhan, and X. Li, "Topology optimization design of automotive suspension control arm," *Engineering Reports*, vol. 7, no. 5, pp. e70188, 2025.

[2] K. Sookchanchai, S. Olarnrithinun, and V. Uthaisangsuk, "Lightweight design of an automotive lower control arm using topology optimization for forming process," *IOP Conference Series: Materials Science and Engineering*, vol. 1157, pp. 012083, 2021.

[3] X. Chen, C. Zhang, and Q. Zhao, "Robust topology optimization of vehicle suspension control arm," *Journal of Beijing Institute of Technology*, vol. 28, no. 3, pp. 626-634, 2019.

[4] D. Gürses, "Optimal design of automobile suspension control arm using metaheuristic algorithms," *International Journal of Automotive Science and Technology*, vol. 9, no. 3, pp. 305-309, 2025.

[5] N. Dhakal, C. Espejo, A. Morina, and N. Emami, "Tribological performance of 3D printed neat and carbon fiber reinforced PEEK composites," *Tribology International*, vol. 193, pp. 109356, 2024.

[6] Z. Hu, J. He, W. Chen, W. Liu, J. Ding, C. He, S. Wang, F. Ning, and X. Li, "High-performance carbon fiber reinforced polyether-ether-ketone composite pellets 3D-printed via screw-extrusion additive manufacturing,"

Composites Science and Technology, vol. 246, pp. 110362, 2023.

[7] D. A. Gök and B. D. Akay, "Fabrication and characterization of carbon and glass fiber reinforced thermoplastic composites by fused filament fabrication," *Scientific Reports*, vol. 15, pp. 30037, 2025.

[8] F. Ning, W. Cong, Y. Hu, and H. Wang, "Additive manufacturing of carbon fiber-reinforced plastic composites using fused deposition modeling: Effects of process parameters on tensile properties," *Journal of Composite Materials*, vol. 51, pp. 451-462, 2017.

[9] S. Lu, B. Zhang, J. Niu, C. Yang, C. Sun, L. Wang, and D. Li, "High-strength carbon fiber-reinforced polyether-ether-ketone composites with longer fiber retention length manufactured via screw extrusion-based 3D printing," *Additive Manufacturing*, vol. 86, pp. 104200, 2024.

[10] J. R. Stojković, R. Turudija, N. Vitković, F. Górski, A. Păcurar, and A. Pleşa, "An experimental study on the impact of layer height and annealing parameters on the tensile strength and dimensional accuracy of FDM 3D printed parts," *Materials*, vol. 16, no. 13, pp. 4574, 2023.

[11] T. L. Ladipo, L. Masu, and P. Nziu, "Mechanical and tribological performance of polyetheretherketone composites using a tabletop 3D printer," *International Journal of Engineering Trends and Technology*, vol. 71, no. 11, pp. 136-147, 2023.

[12] P. Rendas, L. Figueiredo, R. Cláudio, C. Vidal, and B. Soares, "Investigating the effects of printing temperatures and deposition on the compressive properties and density of 3D printed polyetheretherketone," *Progress in Additive Manufacturing*, vol. 9, pp. 1883-1899, 2024.

[13] X. Wang, J. Hu, J. Liu, Y. Liang, L. Wu, T. Geng, S. Liu, and Y. Guo, "Tribological performance and enhancing mechanism of 3D printed PEEK coated with in situ ZIF-8 nanomaterial," *Polymers*, vol. 16, no. 8, pp. 1150, 2024.

[14] E. Komurcu, A. Kefal, M. A. Abdollahzadeh, M. F. Basoglu, E. Kisa, and M. Yildiz, "Towards composite suspension control arm: Conceptual design, structural analysis, laminate optimization, manufacturing, and experimental testing," *Composite Structures*, vol. 327, pp. 117704, 2024.

[15] M. E. Uçak and A. Cengiz, "Independent front suspension lower control arm design with topology optimization approach for electric light-duty vehicle," *International Journal of Automotive Engineering and Technologies*, vol. 14, no. 2, pp. 77-85, 2025.

[16] M. Waqas Arshad, S. Lodi, and D. Q. Liu, "Double wishbone suspension: A computational framework for parametric 3D kinematic modeling and simulation using mathematica," *Technologies*, vol. 13, no. 8, pp. 332, 2025.

[17] U. Ö. Demli and A. Erdem, "Design optimization of armored wheeled vehicle suspension lower control arm," *Materials Testing*, vol. 64, no. 7, pp. 932-944, 2022.

[18] H. L. Tekinalp, V. Kunc, G. M. Velez-Garcia, C. E. Duty, L. J. Love, A. K. Naskar, C. A. Blue, and S. Ozcan, "Highly oriented carbon fiber-polymer composites via additive manufacturing," *Composites Science and Technology*, vol. 105, pp. 144-150, 2014.

[19] N. A. Kadhim, S. Abdullah, A. K. Ariffin, and S. M. Beden, "Fatigue failure behaviour study of automotive lower suspension arm," *Key Engineering Materials*, vol. 462-463, pp. 796-800, 2011.

[20] S. Soydaş, O. Iyibilgin, and H. I. Saraç, "Finite element analysis study: Topology optimization for the front lower arm with innovative double and complex phase materials," *Sustainable Engineering and Innovation*, vol. 6, no. 1, pp. 131-140, 2024.

[21] X. Tang, "Topology optimization design of electric vehicle lower control arm based on SIMP," *Mechanical Research & Application*, vol. 37, no. 6, pp. 99-102, 2024.

[22] B. B. Vatandaş, A. Uşun, N. Yıldız, C. Şimşek, Ö. N. Cora, M. Aslan, and R. Gümrük, "Additive manufacturing of PEEK-based continuous fiber reinforced thermoplastic composites with high mechanical properties," *Composites Part A: Applied Science and Manufacturing*, vol. 167, pp. 107434, 2023.

[23] G. Liu, N. Hu, J. Huang, Q. Tu, and F. Xu, "Experimental investigation on the mechanical and dynamic thermomechanical properties of polyether ether ketone based on fused deposition modeling," *Polymers*, vol. 16, no. 21, pp. 3007, 2024.

[24] A. Awasthi and R. K. Ambikesh, "A review paper on design and analysis of control ARM," *I-Manager's Journal on Mechanical Engineering*, vol. 11, no. 3, pp. 46-52, 2021.

[25] R. Paliwal and R. Shrivastava, "Design and FEA simulation of vehicle suspension system by using ANSYS," *Smart Moves Journal Ijoscience*, vol. 7, no. 11, pp. 32-41, 2021.

[26] S. V. Yende, A. P. Tadamalle, and D. H. Burande, "Topology optimization of lower control arm for LMV," *International Journal of Engineering Research & Technology*, vol. 8, no. 7, pp. 245-249, 2019.

[27] K. Wang, D. S. Yang, and D. W. Ma, "Multi-objective structure optimization design of a car lower control arm," *Advanced Materials Research*, vol. 774-776, pp. 420-427, 2013.

[28] P. Rendas, L. Figueiredo, M. Geraldo, C. Vidal, and B. A. Soares, “Improvement of tensile and flexural properties of 3D printed PEEK through the increase of interfacial adhesion,” *Journal of Manufacturing Processes*, vol. 93, pp. 260-274, 2023.

[29] Ö. Akçay and C. İlkılıç , “Optimum structural design of the lower control arm using meta-heuristic algorithms,” *Journal of the Brazilian Society of Mechanical Sciences and Engineering*, vol. 46, pp. 409, 2024.

[30] T. Hanemann, A. Klein, S. Baumgärtner, J. Jung, D. Wilhelm, and S. Antusch, “Material extrusion 3D printing of PEEK-based composites,” *Polymers*, vol. 15, no. 16, pp. 3412, 2023.